Electronic Supplementary Material (ESI) for Journal of Materials Chemistry A.

Supporting Information

Water-Stable and Hydrophobicity Tunable Organolead Halide Materials with Pb-N Coordination for Electrochemical CO_2 Reduction

Dianxing Ju,[a] Gang Lin,[a] Ming Zhou,[a] Yutao Hua,[a] Xing Li,[a] Huifang Li*[b], and Jian Liu*[a,c]

[a] College of Materials Science and Engineering, Qingdao University of Science and Technology, Qingdao 266042, P.R. China; Email: liujian@qust.edu.cn

[b] College of Electromechanical Engineering, Qingdao University of Science and Technology, Qingdao 266061, P.R. China; Email: huifang0801@gmail.com

[c] Qingdao Institute of Bioenergy and Bioprocess Technology, Chinese Academy of Sciences, Shandong Energy Institute, Qingdao 266101, P.R. China; E-mail: liujian@qibebt.ac.cn

Experimental section

Materials synthesis: All the analytical-grade reactants of PbX_2 (X = Cl, Br, I), Dimethyl sulfoxide(DMSO), 4,4'-Bipyridine (4,4Bpy), 2,2'-Bipyridine (2,2Bpy), oleic acid (OA), oleyl amine (OAm) and 1-octadecene (ODE) were used without further purification. The micron size crystals of $BpyPbX_2$ were synthesized through the reaction of Bpy and PbX_2 precursors in 1-octadecene (ODE) at 140 °C under N_2 atmosphere with the oleyl amine (OAm) and oleic acid (OA) as the surfactants. Typically, for the synthesis of $4{,}4BpyPbI_2$ crystals using 15 mL of ODE, 1 mL of OA, 2 mL of OAm, and PbI_2 (0.001 mol) were loaded into a 100 mL three-necked flask, which was degassed at 120 °C for 30 min, and then heated to 140 °C in 10 min under N_2 flow. Then, the corresponding 4,4Bpy solution (0.001 mol in OAm) was quickly injected. The mixture was kept at 140 °C for 3 h for crystals growth. The resulting products were precipitated using an acetone solution and separated via centrifugation. Others crystals were synthesized with the same process. The larger size crystals were prepared using a temperature lowering method. Briefly, the $BpyPbX_2$ were dissolved in DMSO. Then the mixture was heated to 120 ^{o}C using oil bathing until the reactants dissolved completely. Then the temperature was slow cooled to the room temperature, and the $BpyPbX_2$ crystals were obtained.

X-Ray diffraction measurements: X-ray powder diffraction (XRD) measurements of polycrystalline powder were carried out on a Bruker-AXS D8 Advance X-ray diffractometer with Cu Kα1 radiation (λ = 1.54186 Å) in the range of 5-90° (2θ) with a step size of 0.004°. Structures of single crystals were determined by Bruker SMART APEX-II diffractometer equipped with a CCD detector (graphite-monochromatized Mo Kα radiation, λ = 0.71073 Å) at 176 K. Data integration and cell refinement were performed using the APEX3 software. The structure was analyzed by direct methods and refined using the SHELXTL 97 software package. All nonhydrogen atoms of the structure were refined with anisotropic thermal parameters, and the refinements converged for $Fo^2 > 2\sigma IJFo$. All the calculations were performed using SHELXTL crystallographic software package. Symmetry analysis on the model using PLATON revealed that no obvious space group change was needed.

XPS and UPS measurements: XPS and UPS measurements of the samples with corresponding powder were performed on ESCALAB 250xi (Thermo Fisher Scientific) instrument under vacuum atmosphere (1.7×10^{-10} mbar).

UV-vis diffuse reflectance spectra measurements: UV-vis diffuse reflectance spectroscopy were carried out using a Shimadzu UV 2550 spectrophotometer equipped with an integrating sphere over the spectral range 200-800 nm. A $BaSO_4$ plate was used as the standard (100% reflectance). The absorption spectrum was calculated from the reflectance spectrum using the Kubelka-Munk function: $\alpha/S = (1-R)^2/(2R)$, where α is the absorption coefficient, S is the scattering coefficient, and R is the reflectance. The band gap was calculated using the following function: $(\alpha hv)^2 = B(hv-Eg)$, where α is the absorbance, h is the Planck constant, v is the light frequency, and Eg is the band gap.

PL and TRPL measurements: Photoluminescence measurements were carried out by a laser of 375 nm with a photomultiplier (PMTH-S1-CR131) and DSP lock-in amplifier (SRS 830). The time-resolved photoluminescence measurements were carried by FLS980 all functional fluorescence spectrometer (Edinburgh). The output laser wavelength was 375 nm. The corresponding time-resolved photoluminescence (TRPL) spectra were used to characterize their transport properties, which were fitted by the equation $Y = A + B_1 \exp(-t/\tau_1) + B_2 \exp(-t/\tau_2) + B_3 \exp(-t/\tau_3)$ and included the fast and slow parts.

SEM measurements: Field emission scanning electron microscope (SEM) and energy dispersive spectrometer (EDS) were carried out on Zeiss Sigma-300.

Thermogravimetric analysis Measurements: Differential scanning calorimetry (DSC) and thermogravimetric analysis (TGA) were carried out using a TGA/DSC1/1600HT analyser (METTLER TOLEDO Instruments). The $APbX_2$ (A=4,4Bpy, 2,2Bpy; X=Cl, Br, I) samples were placed in a platinum crucible, and heated at a rate of 10 °C min-1 from room temperature to 800 °C under flowing nitrogen gas. Differential scanning calorimetry (DSC) measurements were implemented on a

NETZSCH DSC 200F3 analyser. The samples were placed in an aluminum crucible with the heating and cooling rates as 5 K/min from 150 K to 300 K in flowing nitrogen.

Photocatalytic reduction of CO_2: The process of CO_2 photoreduction is as follows: The photocatalyst (25 mg) was dispersed into 15 mL water with stirring in the quartz tube, firstly pumped a vacuum of the reaction tube and then bubbled using high purity CO_2 gas, repeated the process for three times to exhaust the air in the tube and filled with enough CO_2 gas. A 25 W LED lamps with 365 nm, 420 nm, 450 nm were applied as the light source. All the photocatalytic process were carried out under the optimum light source, such as $4,4BpyPbCl_2$ and $4,4BpyPbBr_2$ in 365 nm, $4,4BpyPbI_2$ in 420 nm, $2,2BpyPbI_2$ in 450 nm. The gas was collected and monitored via GC-7920 gas chromatograph using flame ionization detector (FID) and thermal conductivity detector (TCD) detectors within a given time interval.

Electrocatalytic reduction of CO_2:

(1) **Preparation of electrodes for CO_2RR in H-cell.** First, 90 mg of conductive carbon cement (SPI Supplies) and 50 mg of catalyst were dispersed in 300 μL thinner. After sonication for 1 h, the catalyst ink was drop cast onto the commercial carbon fiber papers (SGL) of 1×1 cm^2 area, yield the catalyst electrode with different catalyst loading, 3.0 mg cm^{-2}, 5.0 mg cm^{-2}, 8.0 mg cm^{-2}.

(2) **CO_2 electrocatalytic measurements.** The electrochemical CO_2RR analysis was performed in a H-type electrochemical cell separated by a Nafion membrane (N-117, Alfa Aesar), with data collected using a CHI660E electrochemical workstation (Shanghai Chenhua, China). The counter electrode was a carbon rod and the reference electrode was an Ag/AgCl (saturated KCl). The CO_2 saturated 0.5M $KHCO_3$ was used as electrolyte pH=7.70). The gas flow rate was controlled at 25 sccm. The electrode potentials were rescaled to the reversible hydrogen electrode (RHE) using the following equation:

$$E_{RHE} = E_{Ag/AgCl} + 0.197 + 0.0591 \times pH$$

During electrolysis gas was flowed through the cathode compartment of the cell using a mass flow controller (YJ-700CF) and the solution was stirred. The headspace was connected to a gas chromatograph (GC). FE (faradaic efficiency) was calculated based on the time before injection that was required to fill the GC sample injector loops (1 ml). This is summarized in equation for gas product:

$$FE_{gas}\,(\%) = \frac{\mathrm{n \times z \times F}}{\Delta \mathrm{Q}} \times 100$$

Where n is the product measured (mol), z is the number of electrons to make product, F is faradaic constant, ΔQ is the amount of charge during the time the gas enters the GC loops.

n, ΔQ is calculated by the following formula, respectively:

$$\mathrm{n} = \frac{\mathrm{ppm \times P \times V}}{\mathrm{RT}}$$

$$\Delta \mathrm{Q} = \mathrm{Q}_{\mathrm{t=0}} - \mathrm{Q}_{\mathrm{t=x}}$$

Where ppm is the content of product by GC; P is the atmospheric pressure, 101300 Pa; V is the GC sample injector loops, 1 ml; R is the molar gas constant, 8.314 J/(mol·K); T is the room temperature, 298.15 K. $Q_{t=0}$ is the charge passed at the point of injection and $Q_{t=x}$ is the charge passed at x seconds before injection (C), x being the time required to fill the GC sample loop based on sample loop size and gas flow rate.

The concentration of formic acid was estimated by ion chromatograph (863 Basic IC plus. Metrohm, Switzerland) equipped with a Metrosep A Supp 4-250/4.0 column.

$$FE_{HCOO^-}\,(\%) = \frac{n_{HCOO^-} \times 2 \times \mathrm{F}}{\mathrm{Q}} \times 100$$

Where n_{HCOO^-} is the amount of formate determined by the ion chromatography, and F is faradaic constant, Q is the measurement total charge.

Contact angle: The contact angle was measured by LAUDA Scientific Surface Analyser LSA60 at room temperature.

DFT calculations for the water stability of $APbX_2$ crystals: Dispersion-corrected density functional theory (DFT-D3) calculations were carried out with the projector-augmented wave (PAW)[1] based pseudopotential method at the Perdew–Burke–Ernzerhof (PBE)[2] densities functional level and the dispersion corrections were considered (Grimme DFT-D3)[3] for all geometry optimizations. Four-layer (4L) slab models of 4,4BpyPbCl$_2$ (002), 4,4BpyPbBr$_2$ (200), 4,4BpyPbI$_2$ (200) and 2,2BpyPbI$_2$

(200) surface were built and separated by a vacuum space larger than 20 Å. The top two layers (togeter with the water molecular adlayer) were relaxed during geometry optimizations, while the bottom two layers were fixed in their bulk positions obtained from our experimental examination. The plane-wave cutoff was set at 400 eV and a Γ-point-only k-sampling method was adopted for geometry optimizations.[4] An energy convergence criterion of 10^{-6} eV was used and atomic positions were relaxed until the maximal force on each atom was smaller than 0.01 eV A^{-1}. The climbing image-nudged elastic band method (CINEB)[5]was used to examine the diffusion energy barriers of water molecule infiltrates into Pb-X crystal. Calculations were performed with the Vienna *Ab Initio* simulation package[6,7]. The interaction energy of water molecule on the crystal surface was defined as $E_b = E_{water/substrate} - (E_{water} + E_{substrate})$, with $E_{water/substrate}$ being the total energy of the system, E_{water} and $E_{substrate}$ being the total energy of an isolated water molecule and the substrate, respectively.

We performed a series of DFT calculations to investigate the interaction energy of water molecules with $APbX_2$ crystals observed in our experiments. The 4,4Bpy$PbCl_2$ (002), 4,4Bpy$PbBr_2$ (200), 4,4BpyPbI_2 (200) and 2,2BpyPbI_2 (200) surfaces are choosen for our discussion. The geometry optimizations performed for a water molecule adsorbed on the 4,4Bpy$PbCl_2$ (002) surface indicate the presence of ten stable binding sites (see Figure S8). Among them, water molecule located on top of Cl atoms and forming three hydrogen bonds (two Cl…H and one O…H weak interactions, which are 2.33 Å, 2.40 Å and 2.23 Å, respectively) with 4,4Bpy$PbCl_2$ (002) is the most stable one and the adsorption energy is -0.54 eV.

Following the configuration of water molecule located on 4,4Bpy$PbCl_2$ (002) surface, the structure of water molecule on 4,4Bpy$PbBr_2$ (200), 4,4BpyPbI_2 (200) and 2,2BpyPbI_2 (200) surfaces were optimized further. Top view of the optimized geometries are displayed in Figure S8. Calculated interaction energies are given above each panel. Similar with 4,4Bpy$PbCl_2$ (002) case, three hydrogen bonds between water molecule and substrate are formed. Attributed to the different electron affinity of halogen atoms, the bond length between H and Br atoms is longer than H...Cl bond, while is shorter than H...I bond. As a result, the interaction energy of water molecule on 4,4BpyPbBr$_2$ (200) surface is lower by 0.13 eV than on 4,4BpyPbCl$_2$(200) surface. Compared with them, the adsorption energies of water molecule on two I doped APbX$_2$ surfaces are smaller. For 2,2BpyPbI$_2$ (200) and 4,4BpyPbI$_2$ (200), the adsorption energy of water molecule are 0.40 and 0.36 eV, respectively. It means water molecule tends to bind more strongly on 2,2BpyPbI$_2$ (200) than on 4,4BpyPbI$_2$ (200). This should be attributed to the surface configuration of 2,2BpyPbI$_2$ (200) is more preferred for the location of water molecule, see the top and side view of the substrate as shown in Figure S9. As the adsorption energy of water molecule is larger, hydrophobicity of the surface will be weaker. Then, from our theoretical results, it can be concluded that the hydrophobicity of APbX$_2$ surface decreases as an order: 4,4BpyPbCl$_2$ (002) > 4,4BpyPbBr$_2$ (200) > 4,4BpyPbI$_2$ (200) > 2,2BpyPbI$_2$ (200). This is in good agreement with our experimental results.

DFT calculations for the electronic structure of APbX$_2$ crystals: For the electronic character examination of these four Pb-X crystals, a Γ-centered 4 × 4 × 4 k-mesh was used for geometry optimizations and a 8 × 8 × 8 k-mesh was used for the electronic-structure calculations. The plane-wave cutoff was set at 400 eV. An energy convergence criterion of 10^{-6} eV was used for the self-consistent calculations, while atomic positions were relaxed until the maximal force on each atom was smaller than 0.01 eV Å^{-1}.

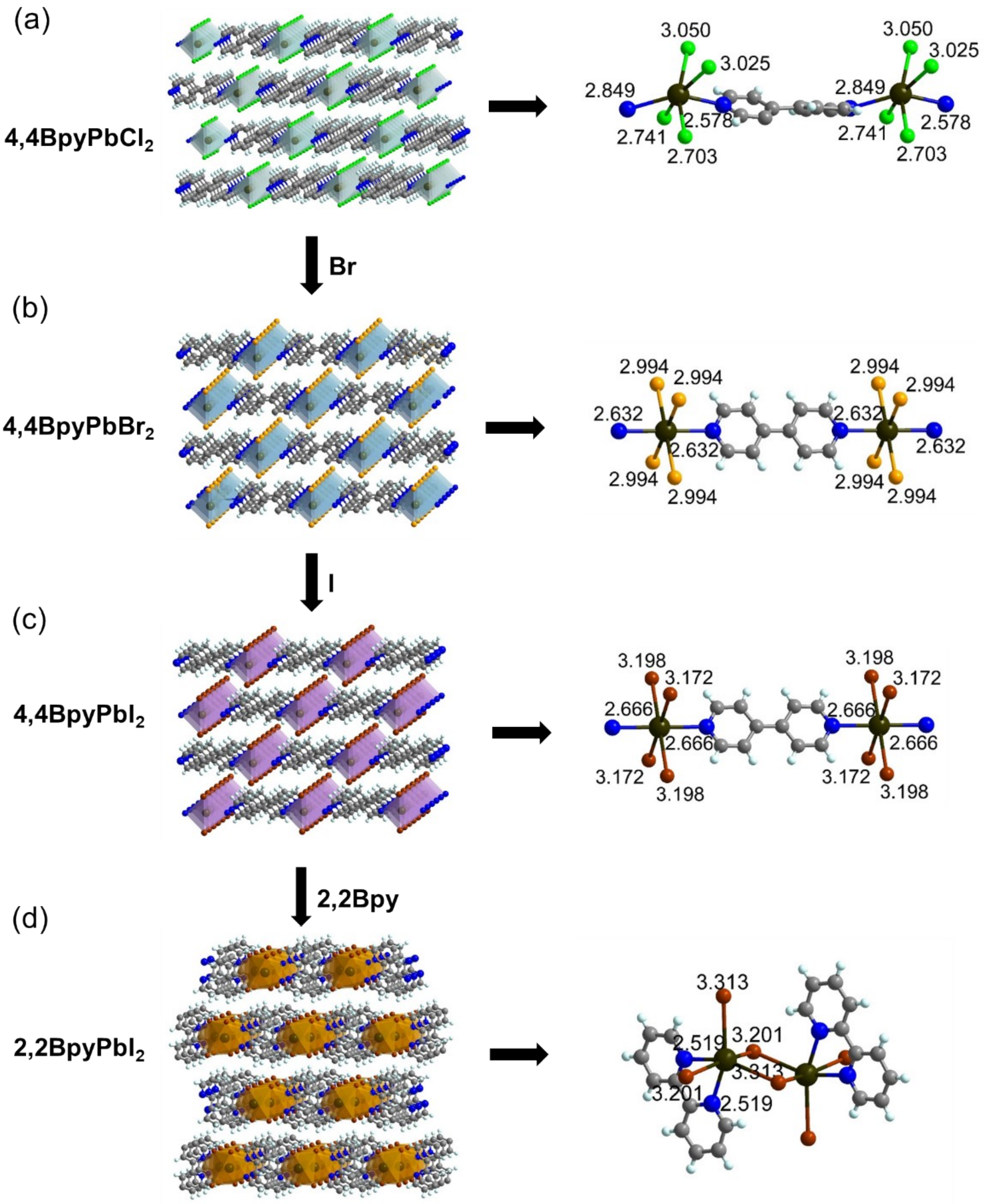

Figure S1. Ball-and-stick diagrams of crystal structures and the [X_4PbN_2] octahedral structure units in $APbX_2$ (A=4,4Bpy, 2,2Bpy; X=Cl, Br, I) crystals. (a) 4,4BpyPbCl_2. (b) 4,4BpyPbBr_2. (c) 4,4BpyPbI_2. (d) 2,2BpyPbI_2. The turquoise, gray, blue, green, orange, brown and olive green represent the atom of H, C, N, Cl, Br, I, and Pb, respectively.

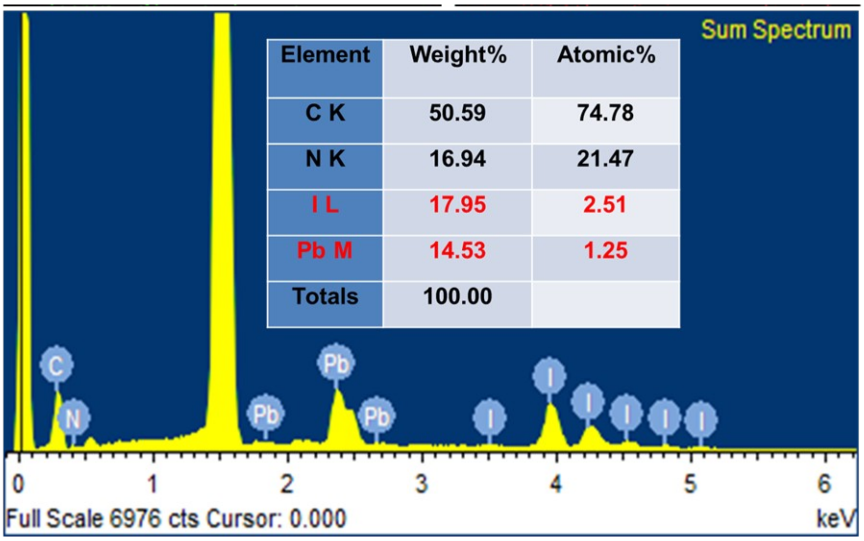

Element	Weight%	Atomic%
C K	50.59	74.78
N K	16.94	21.47
I L	17.95	2.51
Pb M	14.53	1.25
Totals	100.00	

Figure S2. EDS elemental mapping images of 4,4BpyPbI_2.

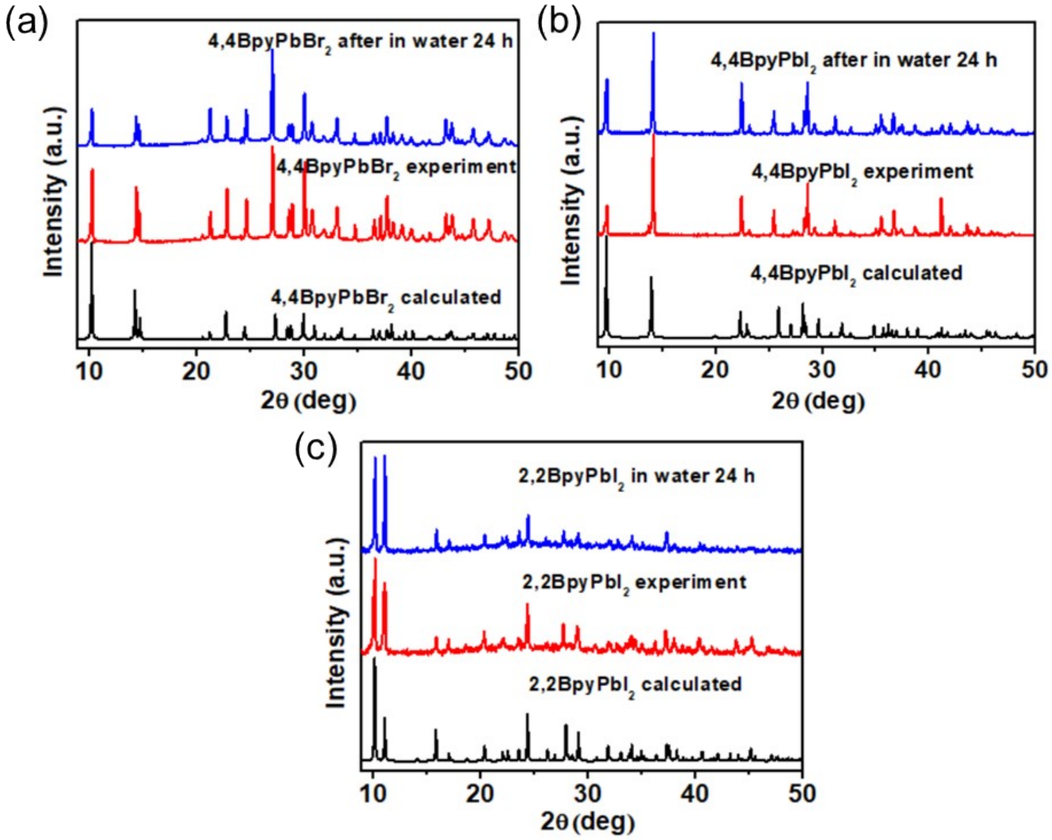

Figure S3. Powder XRD patterns of BpyPbX$_2$ (X= Br, I) before and after soaked in water for 24 h. (a) 4,4BpyPbBr$_2$. (b) 4,4BpyPbI$_2$. (c) 2,2BpyPbI$_2$.

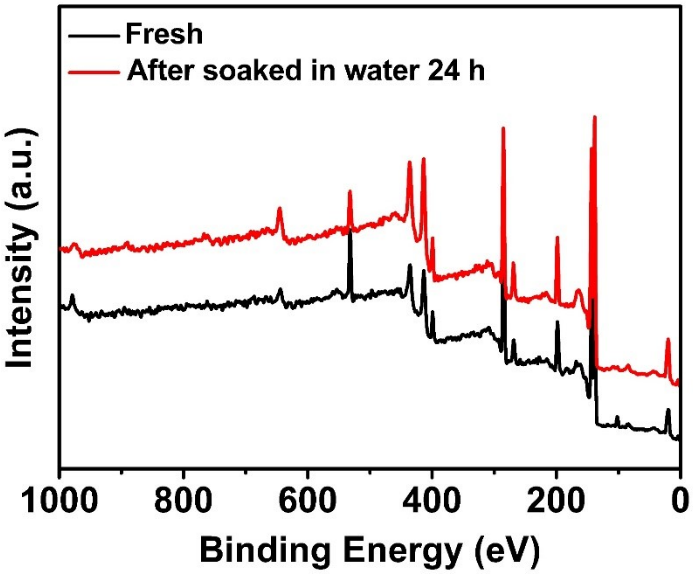

Figure S4. XPS full survey spectrum of 4,4BpyPbCl_2 crystals before and after soaked in water for 24 h.

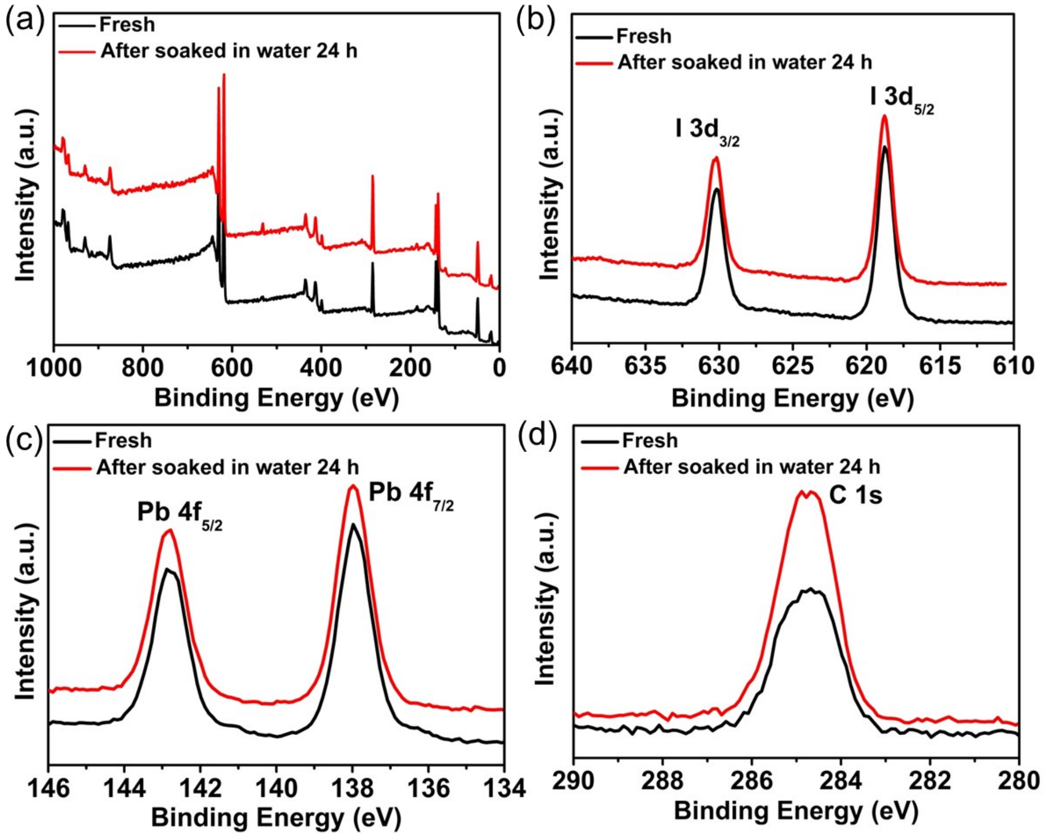

Figure S5. X-ray photoelectron spectra of 4,4BpyPbI$_2$ crystals before and after soaked in water for 24 h. (a) XPS full survey spectrum. (b) I 3d spectrum. (c) Pb 4f spectrum. (d) C 1s spectrum.

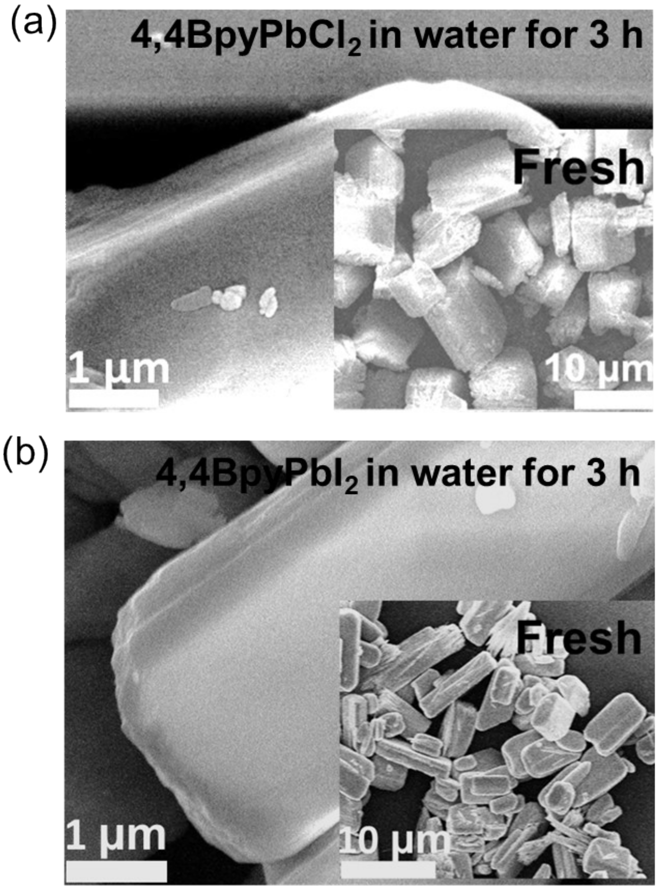

Figure S6. SEM images of (a) 4,4BpyPbCl$_2$ and (b) 4,4BpyPbI$_2$ crystals before and after soaked in water for 24 h.

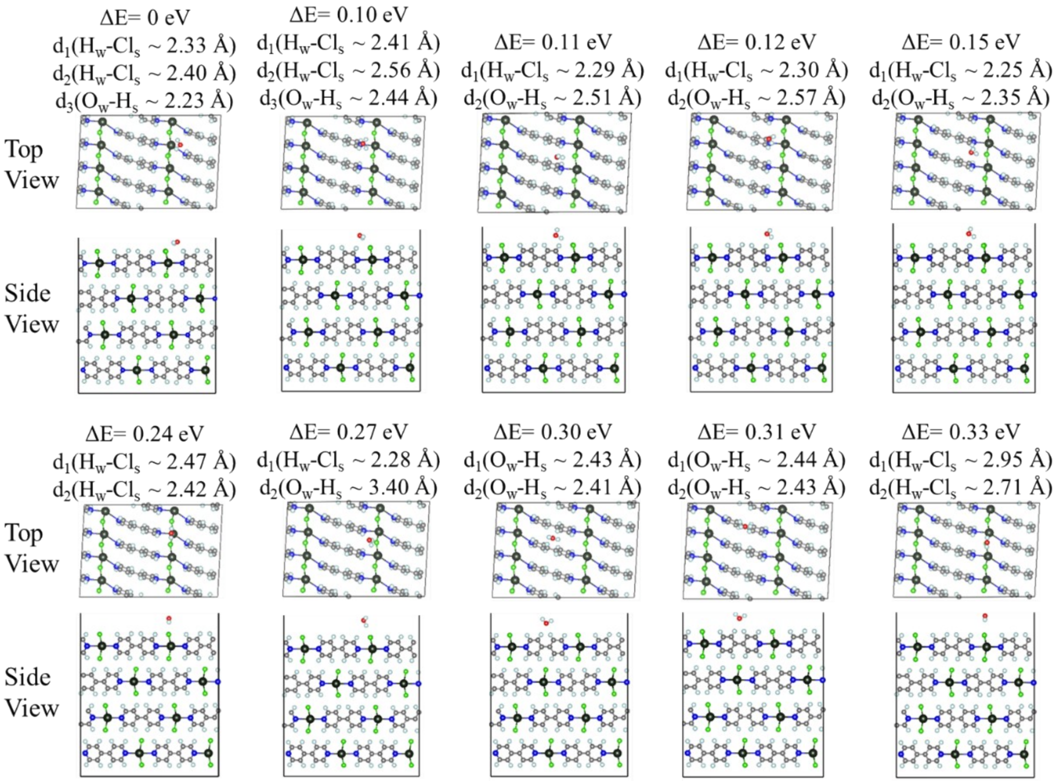

Figure S7. Top and side view of DFT-optimized adsorption geometries of water molecule on 4,4BpyPbCl_2 (002) surface with indication of the interaction energy given above each panel. The turquoise, gray, blue, red, green and olive green represent the atom of H, C, N, O, Cl and Pb, respectively.

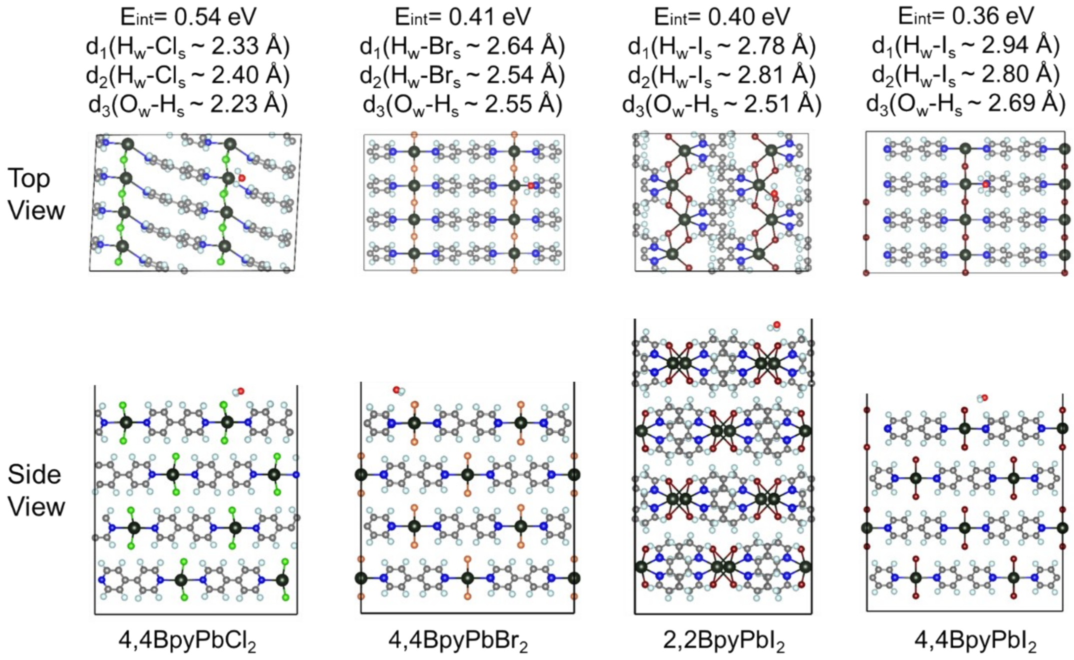

Figure S8. Top and side view of the optimized adsorption geometries of water molecule on 4,4BpyPbCl_2 (002), 4,4BpyPbBr_2 (200), 2,2BpyPbI_2 (200) and 4,4BpyPbI_2 (200) surfaces with indication of the interaction energy given above each panel, as obtained at the PBE-D3 level. The turquoise, gray, blue, red, green, orange, brown and olive green represent the atom of H, C, N, O, Cl, Br, I and Pb, respectively.

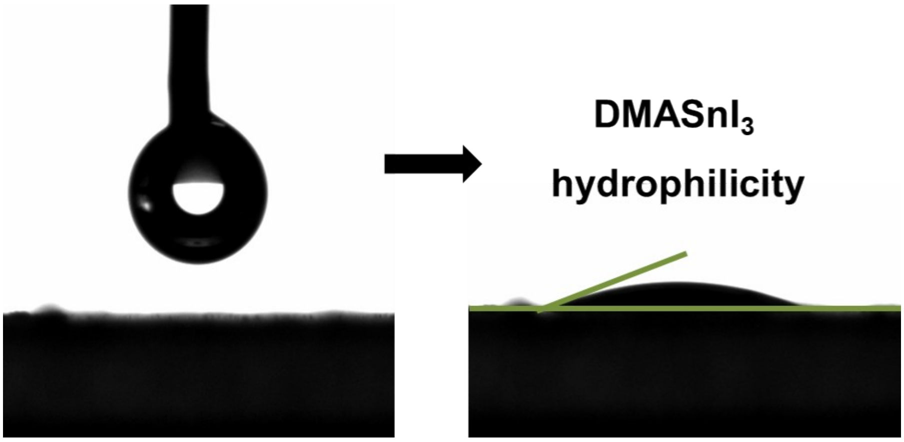

Figure S9. The wettability of $DMASnI_3$.

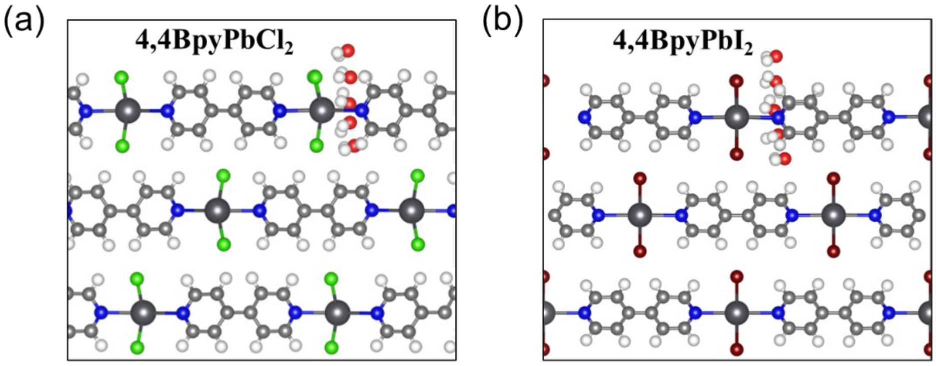

Figure S10. The pathways of one water molecule infiltrate into the subsurface of 4,4BpyPbCl$_2$ (a) and 4,4BpyPbI$_2$ (b) from surface.

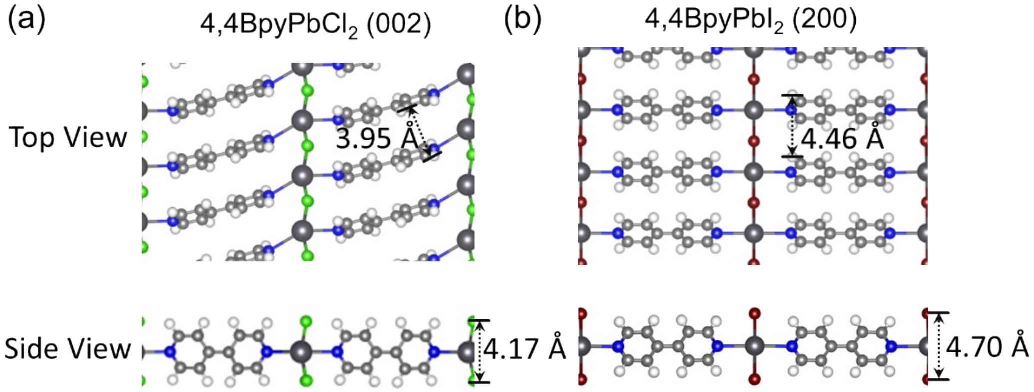

Figure S11. Top view and side view of the top layer of 4,4BpyPbCl$_2$ (a) and 4,4BpyPbI$_2$ (b).

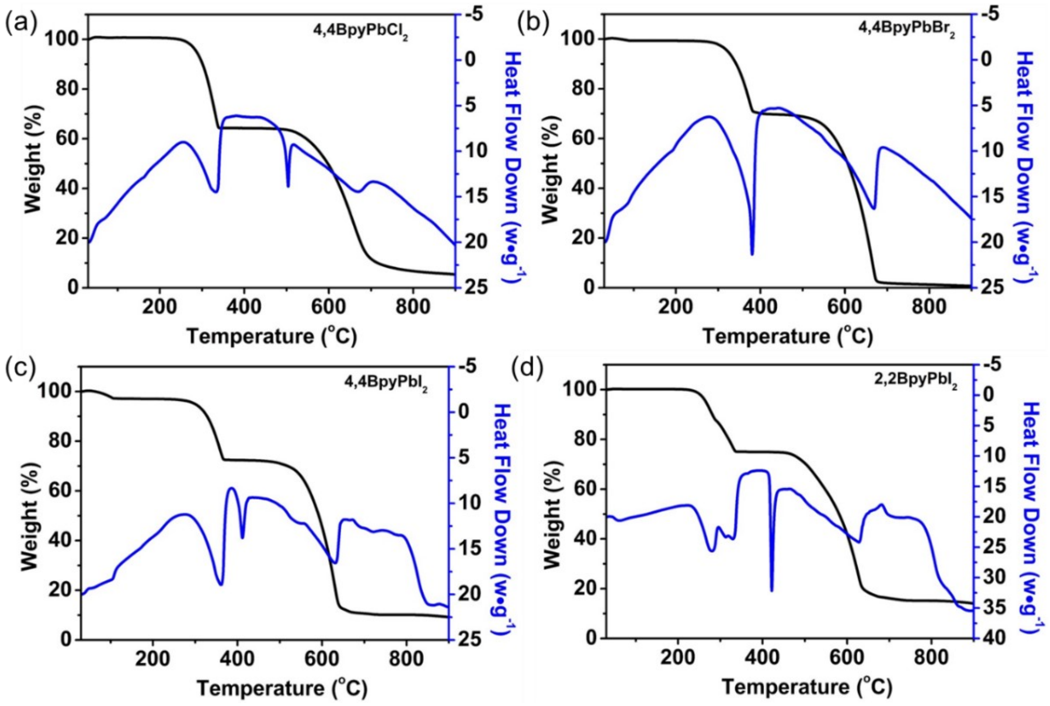

Figure S12. TGA and DSC data for BpyPbX$_2$ (X= Cl, Br, I) crystals. (a) 4,4BpyPbCl$_2$. (b) 4,4BpyPbBr$_2$. (c) 4,4BpyPbI$_2$. (d) 2,2BpyPbI$_2$.

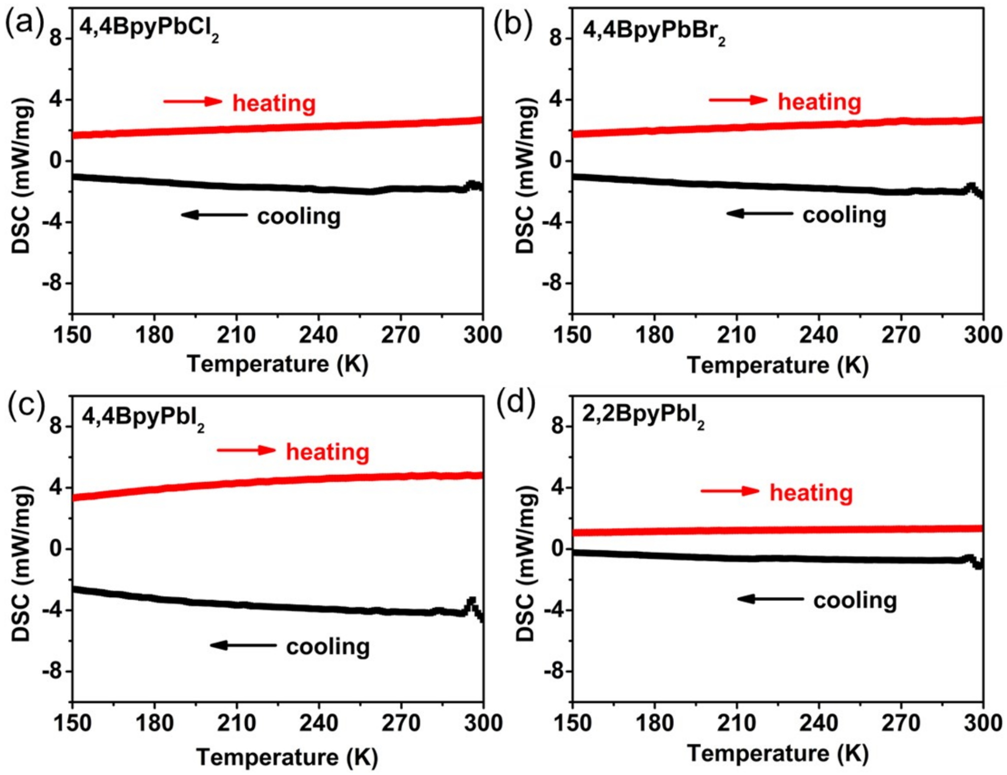

Figure S13. The DSC curves with temperatures ranging from 150 K to 300 K for the following types of $APbX_2$ single crystals. (a) 4,4BpyPbCl_2. (b) 4,4BpyPbBr_2. (c) 4,4BpyPbI_2. (d) 2,2BpyPbI_2.

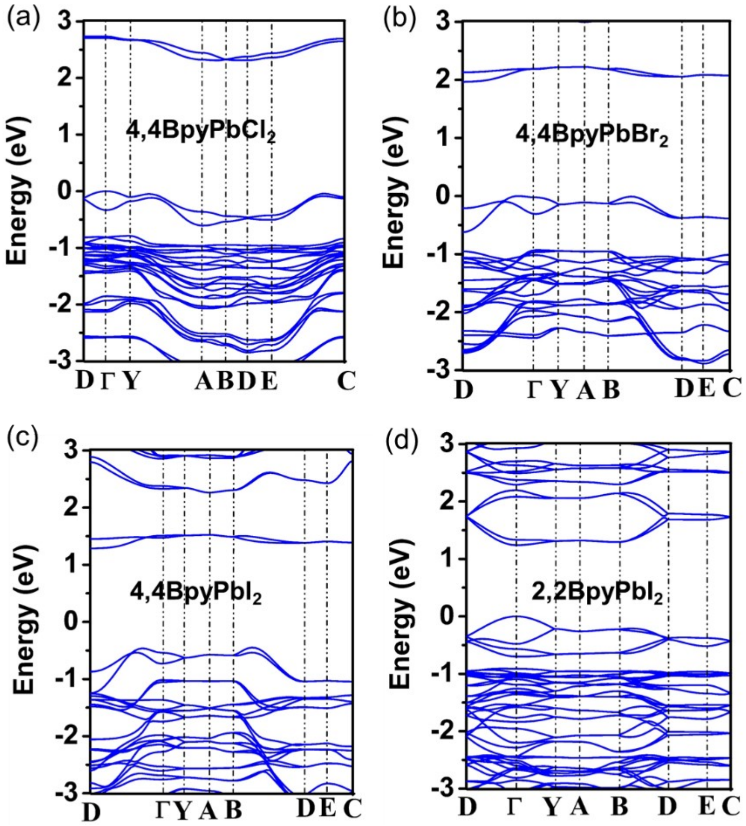

Figure S14. DFT calculations: band structure of APbX$_2$. (a) 4,4BpyPbCl$_2$. (b) 4,4BpyPbBr$_2$. (c) 4,4BpyPbI$_2$. (d) 2,2BpyPbI$_2$.

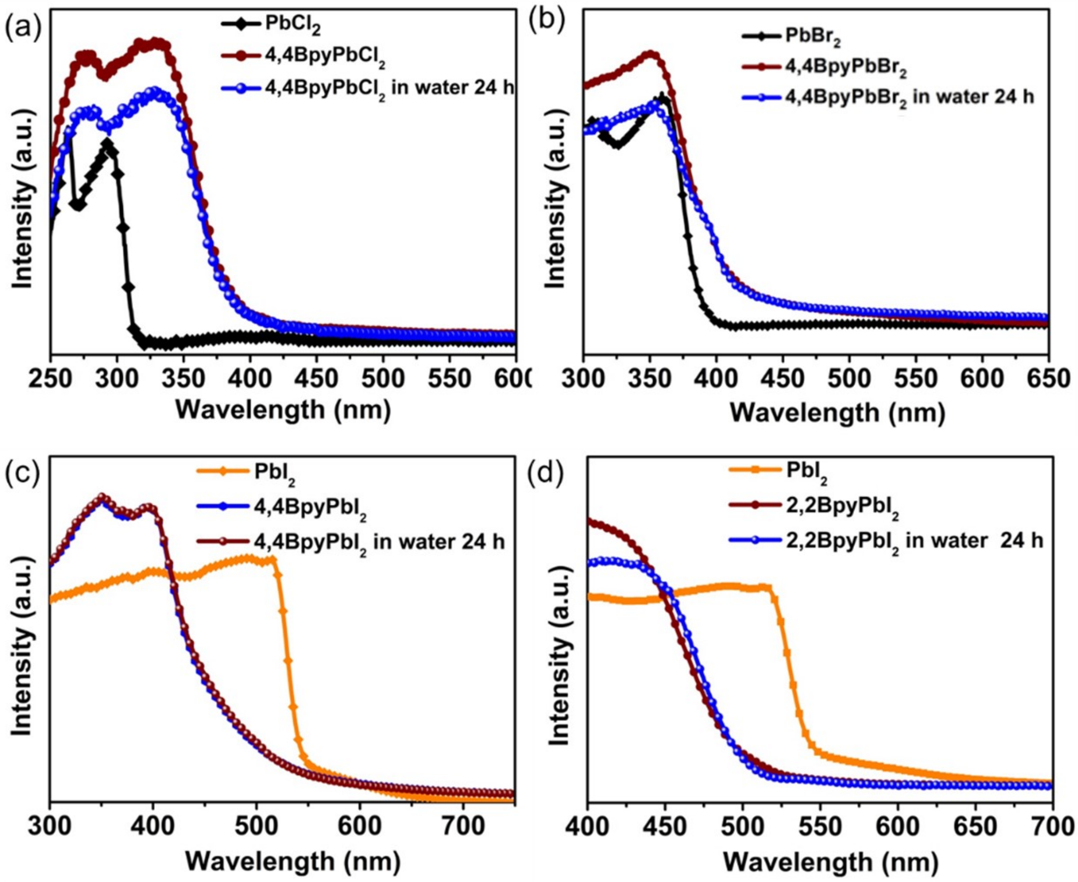

Figure S15. UV-vis diffuse reflectance spectra for $BpyPbX_2$ (X = Cl, Br, I) crystals before and after soaked in water for 24 h. (a) $4,4BpyPbCl_2$, (b) $4,4BpyPbBr_2$, (c) $4,4BpyPbI_2$, (d) $2,2BpyPbI_2$.

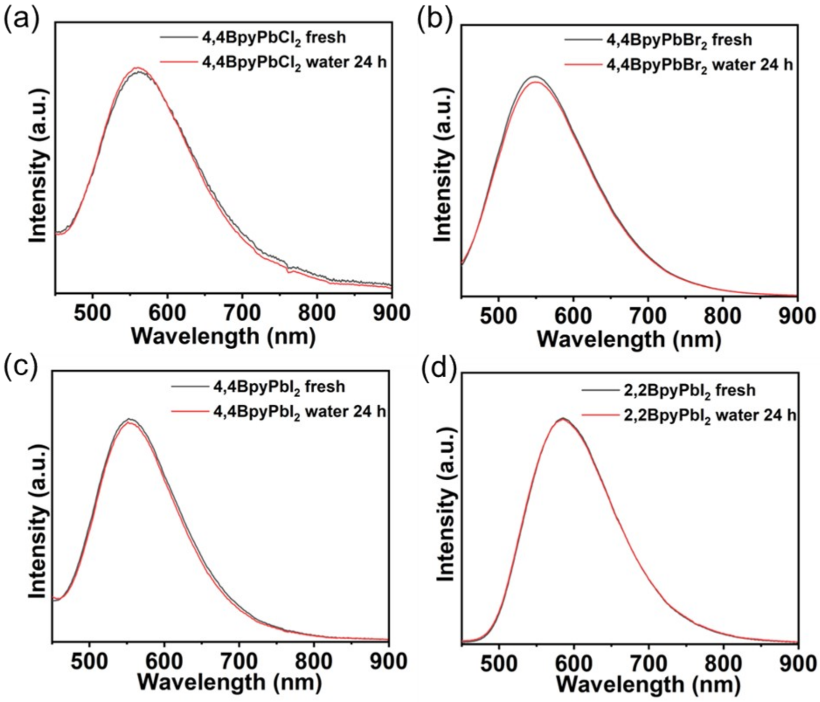

Figure S16. PL spectra for $APbX_2$ crystals before and after soaked in water for 24 h. (a) 4,4BpyPbCl$_2$, (b) 4,4BpyPbBr$_2$, (c) 4,4BpyPbI$_2$, (d) 2,2BpyPbI$_2$.

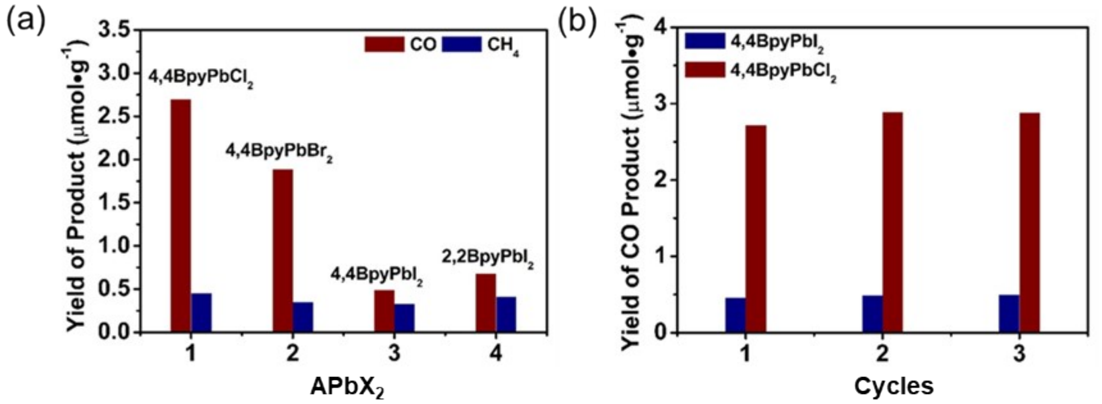

Figure S17. (a) Photocatalytic yields of CO and CH_4 of $APbX_2$ photocatalysts in 3 h. (b) The reproducibility of the production of CO and CH_4 for the 4,4BpyPbCl_2 and 4,4BpyPbI_2 in 3 tests.

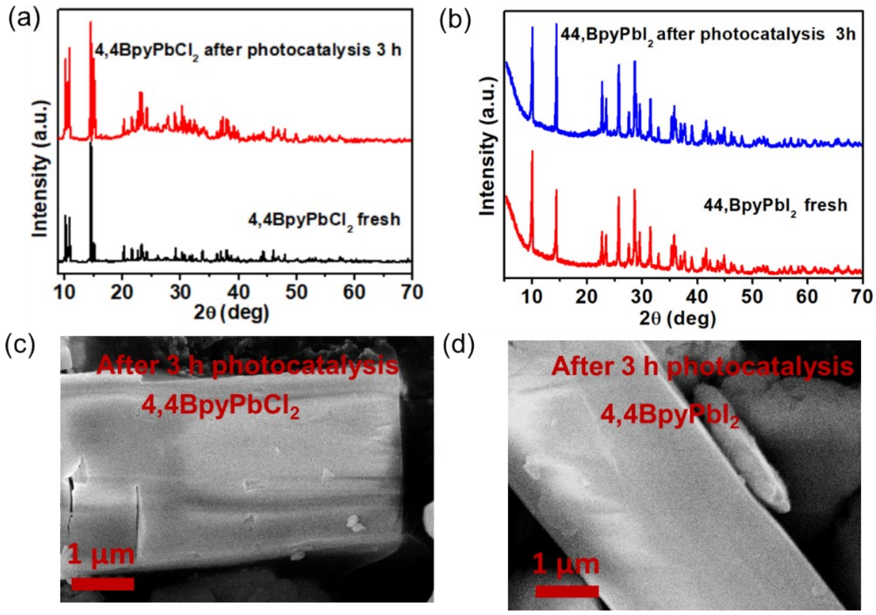

Figure S18. XRD patterns of (a) 4,4BpyPbCl$_2$ and (b) 4,4BpyPbI$_2$ crystals after photocatalytic process for 3 h. SEM images of (c) 4,4BpyPbCl$_2$ and (d) 4,4BpyPbI$_2$ crystals after photocatalytic process for 3 h.

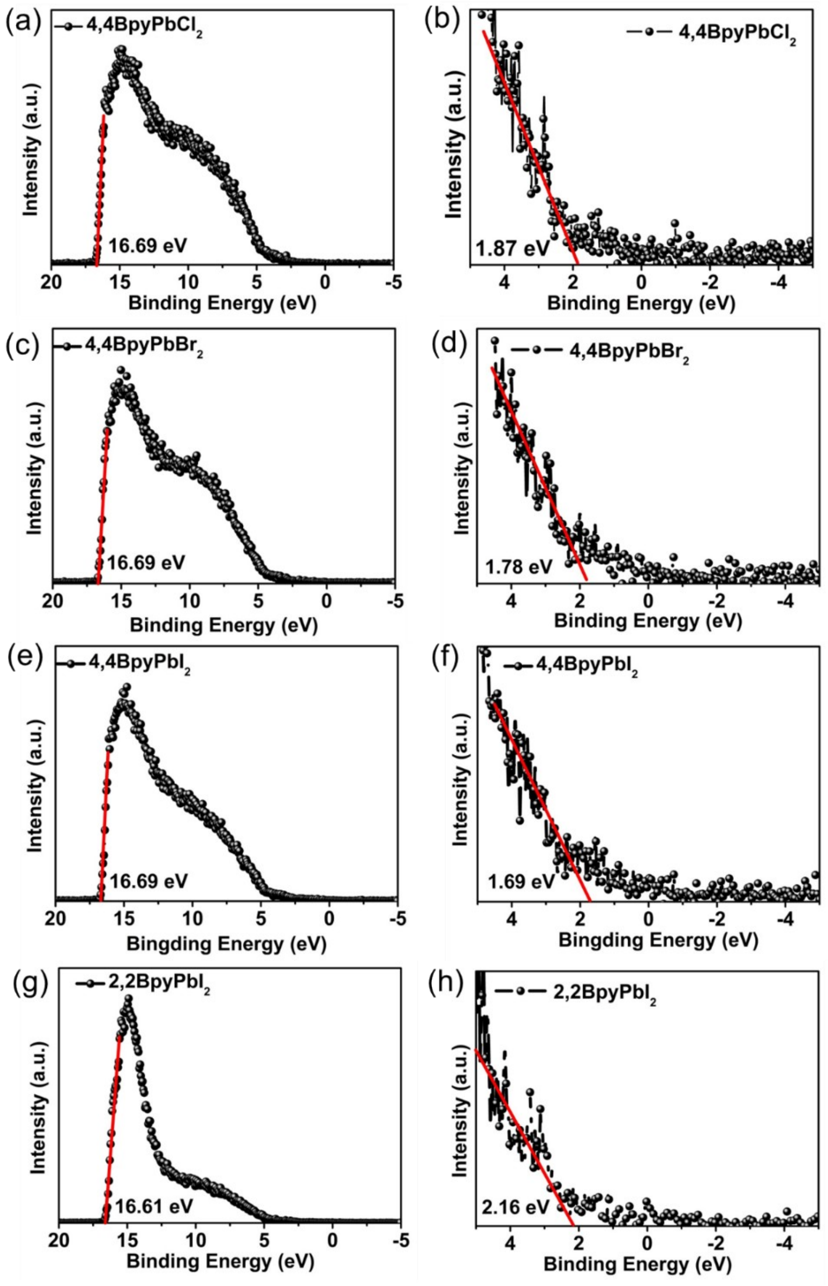

Figure S19 The ultraviolet photoelectron spectra (UPS) of (a, b) 4,4BpyPbCl$_2$. (c, d) 4,4BpyPbBr$_2$. (e, f) 4,4BpyPbI$_2$. (g, h) 2,2BpyPbI$_2$.

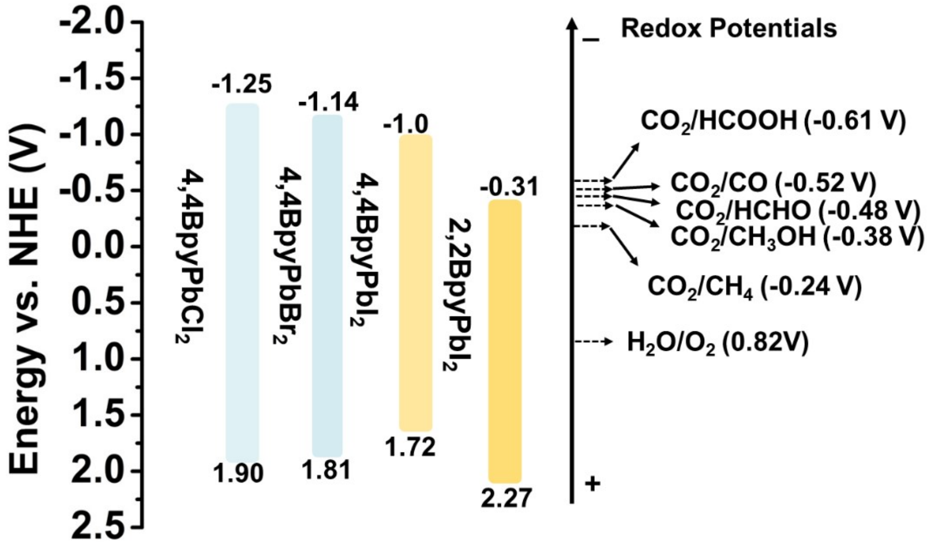

Figure S20. Schematic illustration of the band structures of the NCs derived from the results of UPS and UV-vis absorption spectra.

(a) Conductive Carbon

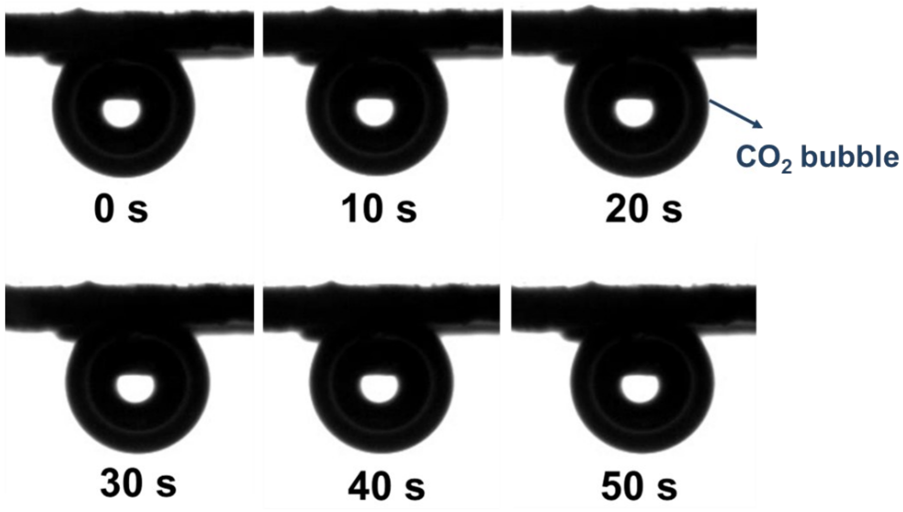

(b) 4,4BpyPbI$_2$ + Conductive Carbon

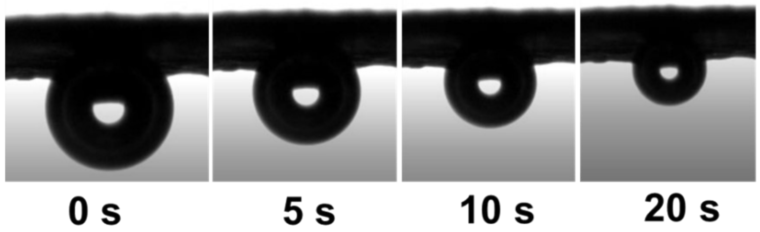

Figure S21. (a) The adsorption behavior of CO$_2$ bubble on conductive carbon. (b) The adsorption behavior of CO$_2$ bubble on conductive carbon electrode including the 4,4BpyPbI$_2$ and conductive carbon.

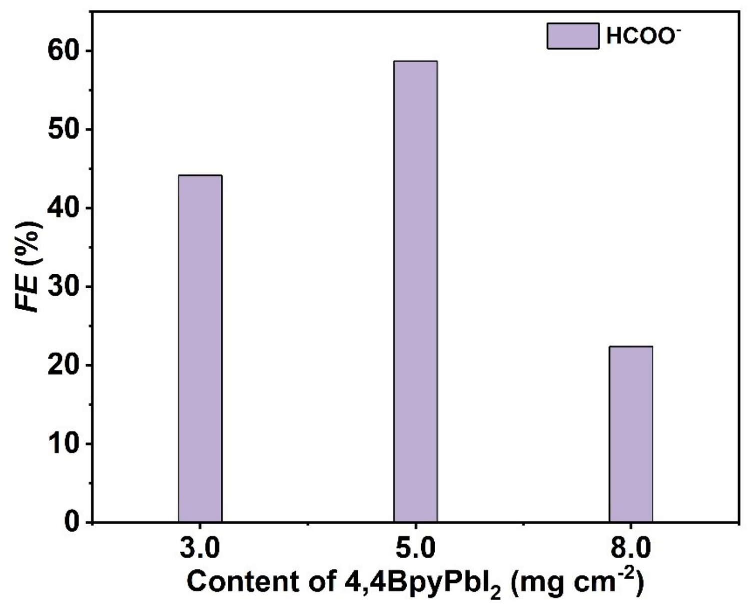

Figure S22. The FE of $HCOO^-$ under the different content of $4,4BpyPbI_2$ at-1.0 V versus RHE in 0.5 M $KHCO_3$.

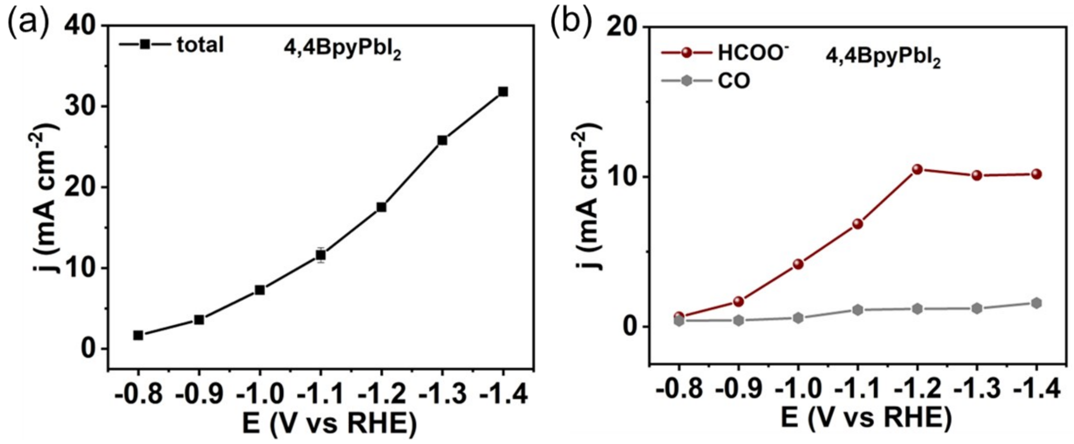

Figure S23. The total current density of electrocatalytic CO_2 reduction at different applied potentials (a) and partial current density of CO_2 reduction products (b).

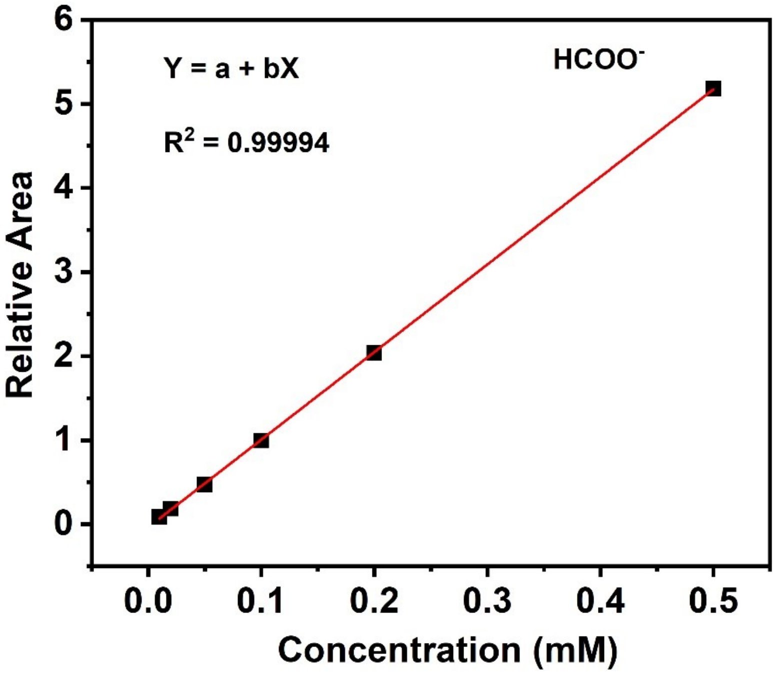

Figure S24. Calibration curves of formate.

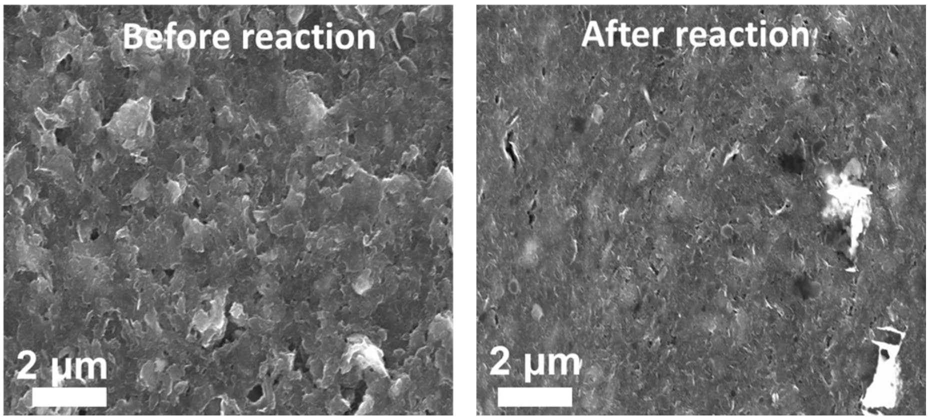

Figure S25. The SEM images of electrode before and after the electrocatalytic reaction.

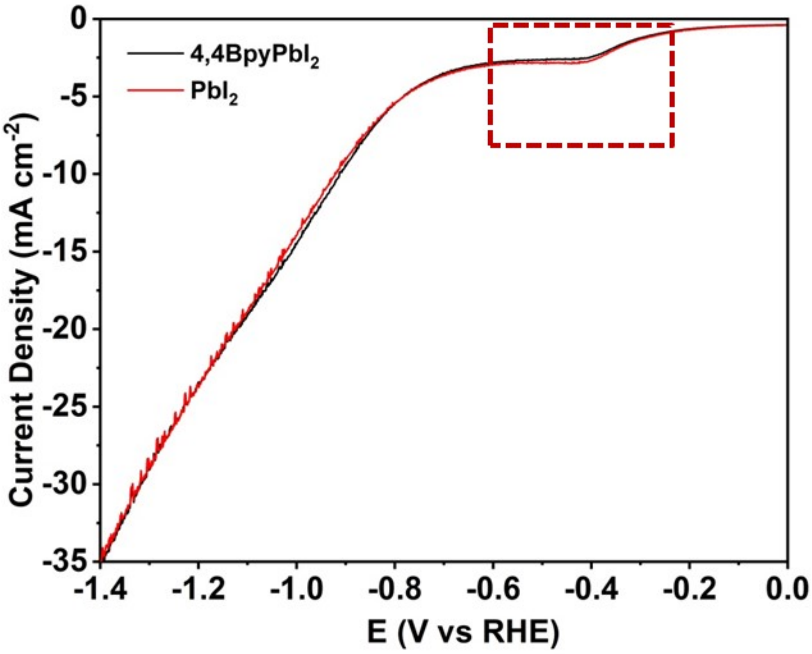

Figure S26. The linear sweep voltammetry curves of 4,4BpyPbI$_2$ and PbI$_2$.

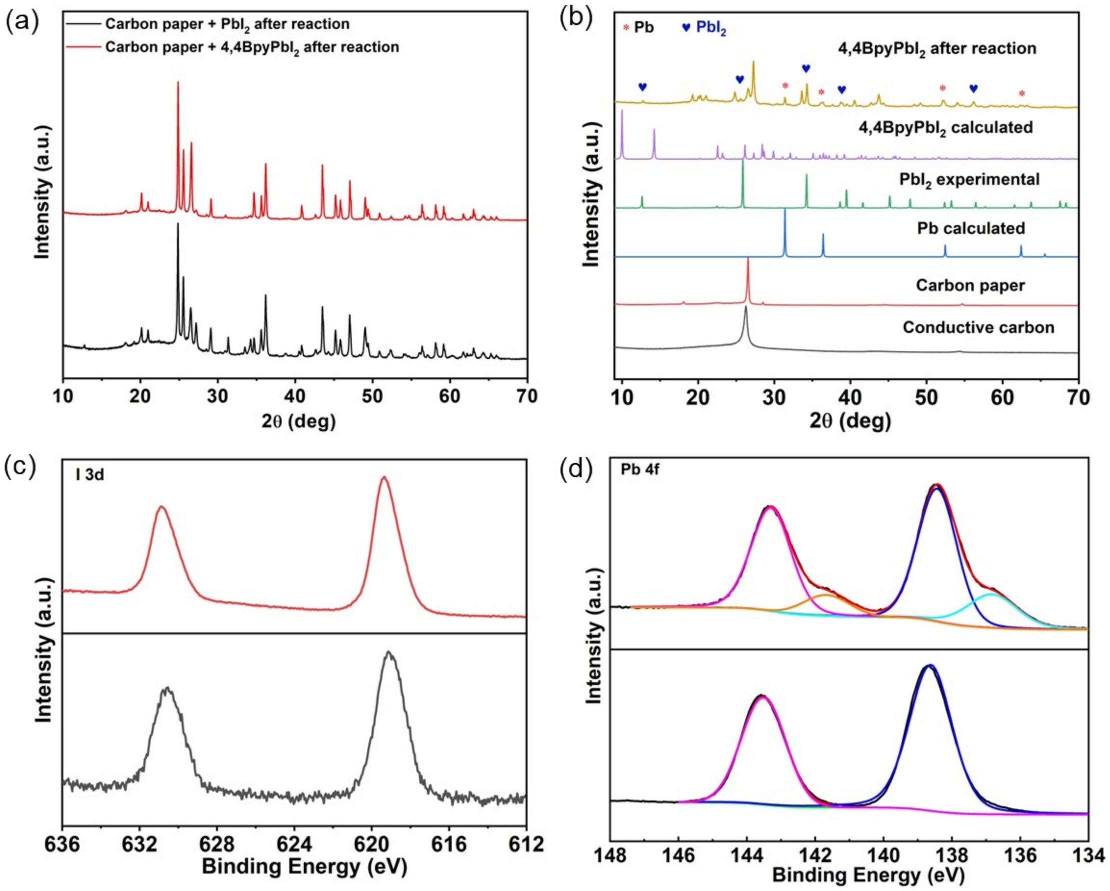

Figure S27. (a, b) The XRD patterns of 4,4BpyPbI_2 and PbI_2 after the electrocatalytic reaction. X-ray photoelectron spectra of PbI_2 after the electrocatalytic reaction. (c) I 3d spectrum. (d) Pb 4f spectrum.

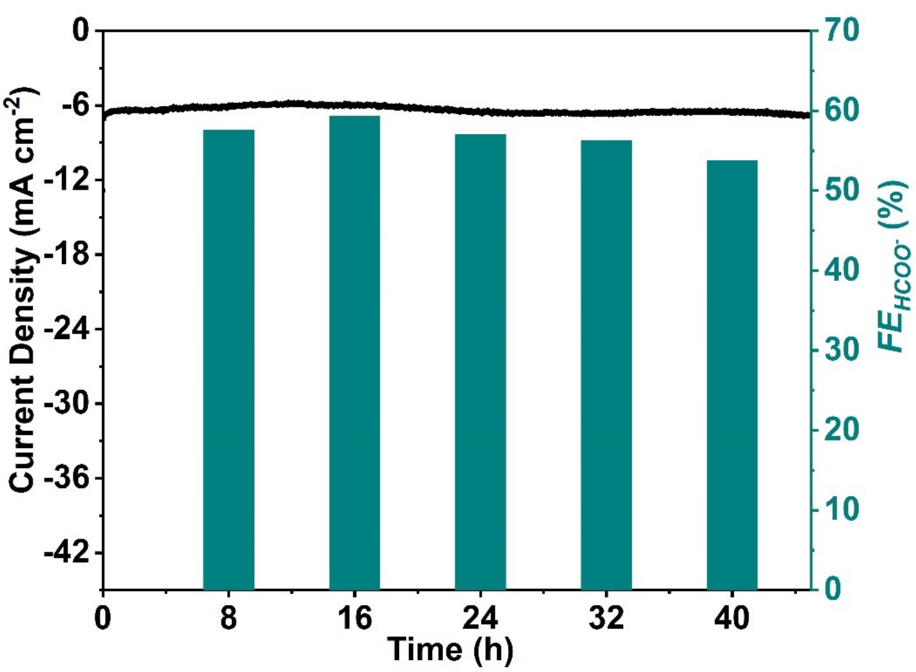

Figure S28. The long-time stability of this catalyst for HCOOH.

Table S1. Crystal data and structure refinement of 4,4BpyPbCl_2, 4,4BpyPbBr_2, 4,4BpyPbI_2 and 2,2BpyPbI_2.

Empirical formula	4,4BpyPbCl_2	4,4BpyPbBr_2	4,4BpyPbI_2	2,2BpyPbI_2
Formula weight/ g·mol^{-1}	434.27	523.19	617.17	617.17
Temperature/K	173	173	173	173
Crystal color	White	White	Yellow	Yellow
Crystal system	triclinic	monoclinic	monoclinic	monoclinic
Space group	P-1	C2/m	C2/m	C2/c
a/Å	3.9454(2)	12.1000(7)	12.6647(5)	16.3113(13)
b/Å	11.8482(13)	12.4041(7)	12.4402(5)	10.3816(7)
c/Å	12.3247(6)	4.2095(2)	4.4277(2)	8.2206(6)
α/°	94.232(4)	90	90	90
β/°	93.267(2)	96.555(4)	97.211(4)	102.375(3)
γ/°	93.132(3)	90	90	90
Volume/Å^3	572.62(7)	627.67(6)	692.07(5)	1359.71(17)
Z	2	2	2	4
Density/g·cm^{-3}	2.519	2.768	2.962	3.015

Table S2. Adsorption energy, hydrogen bond length, and diffusion barrier for the H_2O adsorbed on the $DMASnI_3$, 4,4$BpyPbCl_2$ (002), 4,4$BpyPbBr_2$ (200), 2,2$BpyPbI_2$ (200) and 4,4$BpyPbI_2$ (200) surfaces.

System	**$MAPbI_3$**	**$MASnI_3$**	**$MAGeI_3$**	**$DMASnI_3$**	**4,4$BpyPbCl_2$**	**4,4$BpyPbBr_2$**	**2,2$BpyPbI_2$**	**4,4$BpyPbI_2$**
Adsorption energy (eV)				0.69	0.54	0.41	0.40	0.36
Average hydrogen bond length (Å)	2.6	2.5	1.66	1.7	2.32			
Diffusion barrier from surface to inside (eV)	0.04	0.53	0.09	0.84	1.13			0.98

Table S3. The band gap and lifetimes extracted from the PL spectra of 4,4BpyPbCl_2, 4,4BpyPbBr_2, 4,4BpyPbI_2 and 2,2BpyPbI_2.

Materials	**Band gap (eV)**	**τ_1 (ns)**	**τ_2 (ns)**	**τ_3 (ns)**	**χ^2**
4,4BpyPbCl_2	3.35	0.57	2.89	14.09	1.217
4,4BpyPbBr_2	3.22	502.37	1310.12	--	1.096
4,4BpyPbI_2	2.83	4.37	11.25	--	0.913
2,2BpyPbI_2	2.58	56.21	249.57	--	1.036

Table S4 The FE of formate for 4,4BpyPbI$_2$ obtained from different electrolytes.

	Electrolytes	Gas	FE$_{HCOO^-}$ (%)
1	H_2O	--	0
2	$KHCO_3$ solution	--	0
3	$KHCO_3$ solution	CO_2	19.67
4	N_2 saturated $KHCO_3$	CO_2	19.8
5	N_2 saturated $KHCO_3$	N_2	0
6	Ar saturated $KHCO_3$	CO_2	14.9
7	Ar saturated $KHCO_3$	Ar	0
8	CO_2 saturated $KHCO_3$	CO_2	59.38

References

1. Blöchl, P. E. Projector augmented-wave method. *Phys. Rev. B*, **1994**, *50*, 17953-17979 (1994).

2. Perdew, J. P., Burke, K., Ernzerhof, M. Generalized gradient approximation made simple. *Phys. Rev. Lett.*, **1996**, *77*, 3865-3868.

3. Grimme, S. Semiempirical GGA-type density functional constructed with a long-range dispersion correction. *J. Comput. Chem.,* **2006**, *27*, 1787-1799.

4. Monkhorst, H. J., Pack, J. D. Special points for brillouin-zone integrations. *Phys. Rev. B*, **1996**, ***13***, 5188-5192.

5. Henkelman, G., Uberuaga, B. P., Jónsson, H. A climbing image nudged elastic band method for finding saddle points and minimum energy paths. *J. Chem. Phys.*, *2000*, 113, 9901-9904.

6. Kresse, G., Furthmüller, J. Efficiency of ab-initio total energy calculations for metals and semiconductors using a plane-wave basis set. *Comput. Mater. Sci.*, **1996**, *6*, 15-50.

7. Kresse, G., Furthmüller, J. Efficient iterative schemes for ab initio total-energy calculations using a plane-wave basis set. *Phys. Rev. B*, **1996**, *54*, 11169-11186.

8. Cheng, X.; Dao, X.; Wang, S.; Zhao, J.; Sun, W. Enhanced Photocatalytic CO_2 Reduction Activity over NH_2-MIL-125(Ti) by Facet Regulation, *ACS Catal.*, **2021**, *11*, 650-658.